# Modified tight-binding model for strain effects in monolayer transition metal dichalcogenides

Zhiwei Peng,[1] Zhizi Guan,[2] Hongfei Wang,[1] David J. Srolovitz,[2] and Dangyuan Lei[1,*]
[1]*Department of Materials Science and Engineering, and Centre for Functional Photonics, City University of Hong Kong, Hong Kong 999077, China*
[2]*Department of Mechanical Engineering, University of Hong Kong, Hong Kong 999077, China*

(Received 14 November 2022; revised 24 May 2024; accepted 28 May 2024; published 10 June 2024)

Two-dimensional (2D) transition metal dichalcogenides (TMDCs) have emerged as a materials paradigm for realizing next-generation on-chip electronic and optoelectronic devices. Strain engineering is actively pursued to tune the electronic properties of 2D TMDCs. However, a generalizable, analytical approach for describing the underlying physics of strain effects on band structure is still lacking. Here, we develop a tight-binding model (TBM) that incorporates strain effect to characterize the band structure tuning of TMDC ($MoS_2$, $MoSe_2$, $WS_2$, and $WSe_2$) monolayers under biaxial strain fields; strain-dependent Slater-Koster parameters are employed to describe electron hopping and orbital overlap in the strained monolayers. Our approach follows from the Wills-Harrison suggestions of a linear relationship between biaxial strain and Slater-Koster parameters. This leads to a linear dependence of the electronic band gap on applied strain for both direct-indirect ($MoX_2$) and indirect-direct ($WX_2$) band gap transitions. We further study the influence of biaxial strain on the energy differences between different high-symmetry points in $k$ space to deduce the physical origin of strain-induced variations in the band gap type and size. In this process, we select different TBMs (6- or 11-band) and compare them with different first-principles calculation results (DFT-PBE or DFT-HSE) to demonstrate the effectiveness and completeness of our method. Building on this model, we also examined the changes in effective mass and optical conductivity of TMDCs under strain, offering insights that can aid in the development of practical device applications utilizing these materials. Our investigation may be extended to general strained monolayer TMDCs, paving the way for exploring the electronic properties of nanotubes, wrinkled 2D materials, and van der Waals heterostructures under inhomogeneous strain.

DOI: 10.1103/PhysRevB.109.245412

## I. INTRODUCTION

Two-dimensional (2D) transition metal dichalcogenides (TMDCs), consisting of a transition metal ($M$) atomic layer sandwiched between two chalcogen ($X$) layers, have attracted considerable attention due to their remarkable electronic and optical properties [1]. Their electronic properties may be drastically altered by external strain, allowing control over the performance and optical response of 2D TMDC-based devices [2,3]. Specifically, TMDC band gaps may be decreased (increased) with the application of tensile (compressive) strains [4]. A direct-to-indirect band gap transition occurs at 2% tensile strain in monolayer $MoS_2$ [4], according to theory and recently observed experimentally [5–7]. Most theoretical studies of strain effects in TMDCs rely on density functional theory (DFT) calculations to provide reasonable descriptions of the electronic band structure. While DFT calculations have many advantages, they are not convenient for combination with other effects [8]. The Slater-Koster tight-binding (TB) method was proposed to address the computational difficulties of the linear combination of atomic orbitals method [9]. Cappelluti *et al.* [10] applied the Slater-Koster TB model (TBM) to TMDC monolayers to understand the nature of their band structures; subsequently, spin-orbit coupling (SOC) effects were also included in this approach [11]. Recently, Dias *et al.* [12] developed an improved 11-band TBM to better describe the band structure of the TMDC monolayer by considering the second-nearest-neighbor hopping. Additionally, while there has been commendable work on incorporating the influence of strain on TMDC band structure into the TBM and comparing these with the actual material characteristics, these efforts still exhibit certain limitations and shortcomings. For instance, some early studies merely discussed the potential effects of strain without comparing them with actual first-principles outcomes. Subsequent studies [13], while comparing with DFT results, only presented results under specific strains, and there were notable discrepancies between DFT and TBM outcomes at certain key points that determine the band gap size and type [14]. In other studies, the failure to consider the impact of strain on the Slater-Koster on-site term [15] or to accurately assess its influence on the Slater-Koster parameters led to significant discrepancies from actual outcomes; for instance, a mere 0.04 eV band gap change under 5% strain was reported [16]. To better characterize the band evolution of TMDC monolayers with strain, we propose an improved Slater-Koster TBM based upon strain-dependent Slater-Koster parameters. We believe that the primary contribution of this paper is the development of a slightly improved general TBM. By directly comparing

*Contact author: dangylei@cityu.edu.hk

 

with DFT results, this model offers a more intuitive and accurate depiction of the band structure changes in monolayer TMDCs under strain, making it easier for those interested in this subject to understand and follow. This approach is applicable to efficient predictions in cases where there is defect disorder [17], nonuniform strains [18], and strain-induced bound state [19] or topological phase transitions [20].

This paper is organized as follows. In Sec. II, we propose a Slater-Koster TBM with strain-dependent Slater-Koster parameters and lattice constants for TMDC monolayers that mimic the characteristics of electronic band structures that include SOC. In Sec. III, we compare the band structure, band gap, and energy level of typical high-symmetry points of $k$ space in TMDC monolayers derived from TBM and DFT calculations and show that both 6- and 11-band TBMs capture the main features of the band structure and the trend in the band gap vs strain. In this section, we also use this modified model to predict some strain-level dependent properties of the TMDC monolayer. Finally, we examine the impact of these results and identify future opportunities in Sec. IV.

## II. THEORETICAL APPROACH

### A. Crystal structure

Monolayer TMDCs are composed of three atomic sheets: $X$-$M$-$X$, where the atoms in the transition metal $M$ layer and the two chalcogen $X$ layers all sit on triangular lattice sites, as illustrated in Figs. 1(a) and 1(b). Such TMDC monolayers have a hexagonal 2D Brillouin zone (BZ), as shown in Fig. 1(c), exhibit a direct band gap at the BZ $K$ point $= 4\pi/3a(1, 0)$, a valence band (VB) secondary extremum at the point $\Gamma = (0, 0)$ and a conduction band (CB) secondary extremum at the $Q$ point $\approx 4\pi/3a(\frac{1}{2}, 0)$ (roughly midway between the $\Gamma$ and $K$ points), according to the previous DFT calculations [21,22]. Although DFT calculations provide a comprehensive description of the above characteristics under uniform strain [21,23], they cannot be easily applied to strained samples with wrinkles, systems with a large number of atoms, and some special topological materials [18,24]. Compared with DFT, TBMs have the ability to easily deal with all of these issues [25,26]. In this section, we use the six-band TBM developed by Cappelluti *et al.* [10,11] and the 11-band TBM improved by Dias *et al.* [12] for TMDC monolayers to describe the strain effect in TMDC monolayers.

### B. DFT calculations

The DFT calculations in this paper were performed using VASP [27,28]. The exchange and correlation energy functional is evaluated within the Perdew-Burke Ernzerhof (PBE) approximation [29]. An energy cutoff for the plane-wave basis set was set to 500 eV. All atoms were allowed to fully relax until the forces on each atom are $< 0.005$eV/ Å, and total energy difference is $< 10^{-6}$ eV. For geometry optimization, the BZ is sampled by a Monkhorst-Pack special $k$-point mesh of $15 \times 15 \times 1$. To simulate the 2D sheet structure and remove the spurious interactions between artificial periodic images, a vacuum region of 20 Å is used along the $z$ direction. SOC effects are also considered in the DFT calculation. The biaxial strain is defined as $\epsilon = (a - a_0)/a_0$, where $a_0$ and $a$ represent the lattice constants of unstrained TMDCs and biaxially strained TMDC monolayer, respectively. The unstrained lattice constants adapted in our model are listed in Table I [30,31].

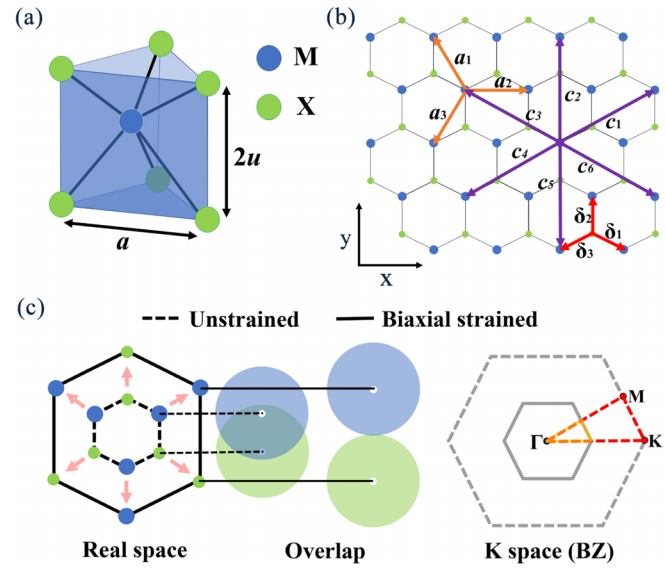


FIG. 1. (a) Lattice structure of the transition metal dichalcogenide (TMDC) $MX_2$ unit cell. $a$ and $u$ represent the lattice constant and the distance between the transition metal and chalcogen layers. (b) Top view of the monolayer $MX_2$ lattice array. $\vec{\delta}_i$, $\vec{a}_i$, and $\vec{c}_i$ are the vectors to represent nearest-neighbor ($M$-$X$) hopping processes, same-type-atom nearest-neighbor ($M$-$M$ and $X$-$X$) hopping processes, and same-type-atom second-nearest neighbors ($M$-$M$ and $X$-$X$), respectively. (c) Schematic of the effects of biaxial strain on the lattice structure, electron wave function overlap, and the Brillouin zone (BZ). In the case of tensile biaxial strain, the distances between the atoms increases in all orientations. The larger distance weakens electron wave function overlap, shrinks the BZ, and shifts the high-symmetry points in the $k$ space accordingly.

### C. Six-band TBM

As shown in Fig. 2, DFT calculations including the SOC effect indicate that chalcogen-atom ($X$) $p$ orbitals ($p_x$, $p_y$, and $p_z$) and transition-metal-atom ($M$) $d$ orbitals ($d_{3z^2\text{-}r^2}$, $d_{yz}$, $d_{xz}$, $d_{x^2\text{-}y^2}$, and $d_{xy}$) dominate the CBs and VBs of TMDC monolayers [10]. Hence, a Hilbert space defined by an 11-fold vector describes five $d$ orbitals of the $M$ atom and six $p$ orbitals of two $X$ atoms in a unit cell [10]:

$$\Psi = \left(p_x^t, p_y^t, p_z^t, d_{3z^2\text{-}r^2}, d_{yz}, d_{xz}, d_{x^2\text{-}y^2}, d_{xy}, p_x^b, p_y^b, p_z^b\right), \quad (1)$$

TABLE I. Lattice constants of unstrained TMDC monolayers used for DFT calculations. $a_0$ represents the unstrained lattice constant, and $u$ represents the distance between transition metal and chalcogen layers. All parameters are in Å units.

| | $a_0$ (Å) | $u$ (Å) |
|---|---|---|
| $MoS_2$ monolayer | 3.160 | 1.586 |
| $WS_2$ monolayer | 3.153 | 1.571 |
| $MoSe_2$ monolayer | 3.288 | 1.644 |
| $WSe_2$ monolayer | 3.282 | 1.641 |

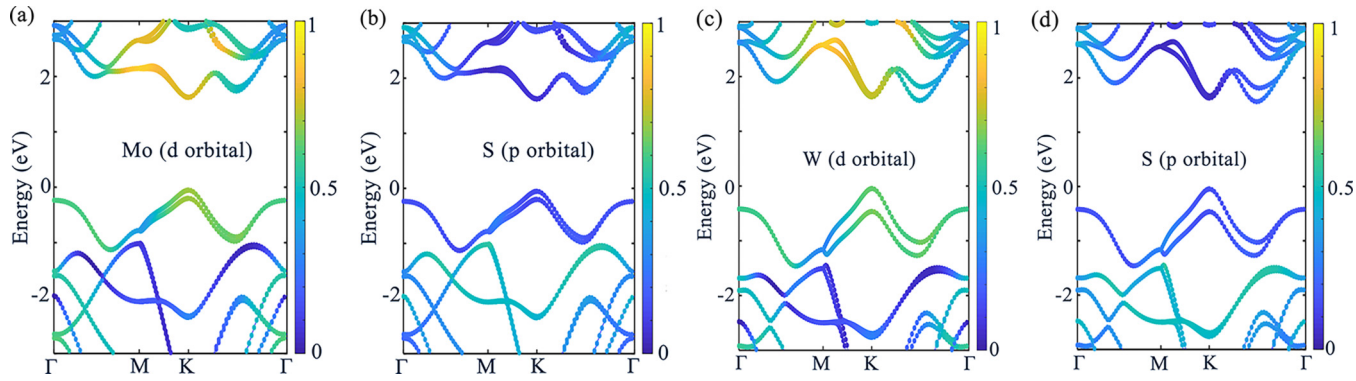


FIG. 2. Orbital-projected monolayer $MoS_2$ and $WS_2$ band structure obtained by density functional theory (DFT) calculations. (a) Orbital-projected band structure for Mo-atom $4d$ orbitals and (b) S-atom $3p$ orbitals in $MoS_2$. (c) Orbital-projected band structure for W-atom $5d$ orbitals and (d) S-atom $3p$ orbitals in $WS_2$. Band color represents orbital weight.

where $t$ and $b$ refer the chalcogen atoms in the top and bottom layers. A TBM can be constructed based upon the hopping integrals between different orbitals of nearest neighbors. These may be determined from the Slater-Koster parameters corresponding to $\sigma$, $\delta$, and $\pi$ ligands [9] ($V_{pd\sigma}, V_{pd\pi}$ for $M$-$X$ bonds, $V_{dd\sigma}, V_{dd\pi}, V_{dd\delta}$ for $M$-$M$ bonds, and $V_{pp\sigma}, V_{pp\pi}$ for $X$-$X$ bonds; in the subscripts, $p, d$ stand for the $p, d$ orbitals in the corresponding atoms, while $\sigma, \pi$, and $\delta$ denote the manner in which electron clouds overlap between different orbitals, namely, the bond type). Five on-site parameters related to the crystal field ($\Delta_0$, $\Delta_1$, $\Delta_2$, $\Delta_p$, and $\Delta_z$) are required in this model to describe the energies of atomic levels $l = 0$ ($d_{3z^2\text{-}r^2}$), 1 ($d_{yz}, d_{xz}$), and 2 ($d_{x^2-y^2}, d_{xy}$) orbitals of the $M$ atom and in-plane ($p_x, p_y$) and out-plane ($p_z$) orbitals of the $X$ atom. By introducing the linear symmetric and antisymmetric combinations of $X$-atom $p$ orbitals (note the inversion of $z \to -z$), the Hilbert space may be represented as [10]

$$\Psi = \left(d_{3z^2\text{-}r^2}, d_{x^2\text{-}y^2}, d_{xy}, p_x^S, p_y^S, p_z^A\right), \tag{2}$$

where $p_i^S = (p_i^t + p_i^b)/\sqrt{2}$ and $p_i^A = (p_i^t - p_i^b)/\sqrt{2}$, with $i = x, y, z$, correspond to the symmetric and antisymmetric combinations, respectively. According to the above reduced Hilbert basis, the TBM Hamiltonian in real space is

$$H = \sum_{i,\mu\nu} \Delta_{\mu,\nu} c_{i,\mu}^\dagger c_{i,\nu} + \sum_{ij,\mu\nu} [t_{ij,\mu\nu} c_{i,\mu}^\dagger c_{j,\mu} + \text{H. c.}], \tag{3}$$

where $c_{i,\mu}^\dagger (c_{i,\nu})$ represents the creation (annihilation) of an electron in orbitals $\mu(\nu) = 1, \ldots, 6$ related to Eq. (2) in the $i$ unit cell, $t_{ij,\mu\nu}$ are the hopping terms, and H.c. is the abbreviation of Hermitian conjugate. Employing a Fourier transformation, the Hamiltonian in $k$ space maybe be expressed as [11]

$$\mathcal{H} = \begin{pmatrix} \mathcal{H}_{MM} & \mathcal{H}_{MX} \\ \mathcal{H}_{MX}^\dagger & \mathcal{H}_{XX} \end{pmatrix}, \tag{4a}$$

$$\mathcal{H}_{MM} = \Delta_M + 2 \sum_{i=1,2,3} t_i^{MM} \cos(\vec{k} \cdot \vec{a}_i), \tag{4b}$$

$$\mathcal{H}_{XX} = \Delta_X + 2 \sum_{i=1,2,3} t_i^{XX} \cos(\vec{k} \cdot \vec{a}_i), \tag{4c}$$

$$\mathcal{H}_{MX} = \sum_{i=1,2,3} t_i^{MX} \exp(-i\vec{k} \cdot \vec{\delta}_i), \tag{4d}$$

where vector $\vec{\delta}_i$ represents the nearest neighbors ($M$-$X$):

$$\vec{\delta}_1 = \left(\frac{a}{2}, \frac{-\sqrt{3}a}{6}, \pm u\right),$$

$$\vec{\delta}_2 = \left(0, \frac{\sqrt{3}a}{3}, \pm u\right),$$

$$\vec{\delta}_3 = \left(\frac{-a}{2}, \frac{-\sqrt{3}a}{6}, \pm u\right), \tag{5}$$

and vector $\vec{a}_i$ corresponds to same-type-atom nearest neighbors ($M$-$M$ or $X$-$X$):

$$\vec{a}_1 = \left(\frac{-a}{2}, \frac{\sqrt{3}a}{2}, 0\right),$$

$$\vec{a}_2 = (a, 0, 0),$$

$$\vec{a}_3 = \left(\frac{-a}{2}, \frac{-\sqrt{3}a}{2}, 0\right). \tag{6}$$

More details on the Hamiltonian are provided in Appendix A.

### D. 11-band TBM

To have a more accurate description of the band structure of a TMDC monolayer, we also referred to the 11-band TBM developed by Dias *et al.* [12], which considers the second-nearest-neighbor hopping. This model did not reduce the basis but divided it into two categories based on its parity, namely, the even part [$d_{z^2}$, $d_{xy}$, $d_{x^2\text{-}y^2}$, $p_z^e = (p_z^t - p_z^b)/\sqrt{2}$, $p_x^e = (p_x^t + p_x^b)/\sqrt{2}$, $p_y^e = (p_y^t + p_y^b)/\sqrt{2}$] and odd part [$d_{xz}$, $d_{yz}$, $p_z^o = (p_z^t + p_z^b)/\sqrt{2}$, $p_x^o = (p_x^t - p_x^b)/\sqrt{2}$, $p_y^o = (p_y^t - p_y^b)/\sqrt{2}$]. Hence, the Hilbert space is on the basis of the 11-fold vector:

$$\Psi = \left(d_{z^2}, d_{xy}, d_{x^2\text{-}y^2}, p_z^e, p_x^e, p_y^e, d_{xz}, d_{yz}, p_z^o, p_x^o, p_y^o\right). \tag{7}$$

In this way, the Hamiltonian matrix elements will be decoupled into two parts, the $6 \times 6$ block based on the even basis set and $5 \times 5$ block associated with the odd basis set, which is

given by

$$\mathcal{H}_{\mathrm{TB}} = \begin{pmatrix} \mathcal{H}_E & 0 \\ 0 & \mathcal{H}_O \end{pmatrix}, \tag{8}$$

where $\mathcal{H}_{E/O}$ represent the elements associated with the even/odd part. Furthermore, $\mathcal{H}_{E/O}$ is defined by

$$\mathcal{H}_{E/O} = \begin{pmatrix} M^{E/O} + \mathcal{H}_{M-M}^{E/O} & \mathcal{H}_{M-X}^{E/O} \\ \mathcal{H}_{M-X}^{E/O\ \dagger} & X^{E/O} + \mathcal{H}_{X-X}^{E/O} \end{pmatrix},$$

$$M^E = \begin{pmatrix} E_{d_0}^e & 0 & 0 \\ 0 & E_{d_1}^e & 0 \\ 0 & 0 & E_{d_1}^e \end{pmatrix},$$

$$M^O = \begin{pmatrix} E_{d_2}^o & 0 \\ 0 & E_{d_2}^o \end{pmatrix},$$

$$X^E = \begin{pmatrix} E_{s_2}^e & 0 & 0 \\ 0 & E_{s_1}^e & 0 \\ 0 & 0 & E_{s_1}^e \end{pmatrix},$$

$$X^O = \begin{pmatrix} E_{s_2}^e & 0 & 0 \\ 0 & E_{s_1}^e & 0 \\ 0 & 0 & E_{s_1}^e \end{pmatrix}. \tag{9}$$

in which $M^{E/O}$ and $X^{E/O}$ are the matrix elements associated with the on-site energy, and $\mathcal{H}_{M\text{-}M}^{E/O}$, $\mathcal{H}_{X\text{-}X}^{E/O}$, and $\mathcal{H}_{M\text{-}X}^{E/O}$ are the hopping matrices between same kinds of atoms ($M$-$M$, $X$-$X$) and different types of atoms ($M$-$X$), respectively. By considering the second-nearest neighbor, the hopping matrices are defined by

$$\mathcal{H}_{M\text{-}X}^{E/O} = \sum_{i=1}^{3} \exp(i\vec{k}\cdot\vec{a}_i)\mathcal{H}_{M\text{-}X}^{E/O}(\vec{a}_i),$$

$$\mathcal{H}_{M\text{-}M}^{E/O} = \sum_{i=1}^{6} \exp(i\vec{k}\cdot\vec{\delta}_i)\mathcal{H}_{M}^{E/O}(\vec{\delta}_i) + \sum_{i=1}^{6} \exp(i\vec{k}\cdot\vec{c}_i)\mathcal{H}_{M}^{E/O}(\vec{c}_i),$$

$$\mathcal{H}_{X\text{-}X}^{E/O} = \mathcal{H}_{tb}^{E/O} + \sum_{i=1}^{6} \exp(i\vec{k}\cdot\vec{\delta}_i)\mathcal{H}_{X}^{E/O}(\vec{\delta}_i),$$

$$+ \sum_{i=1}^{6} \exp(i\vec{k}\cdot\vec{c}_i)\mathcal{H}_{X}^{E/O}(\vec{c}_i). \tag{10}$$

in which $tb$ indicates the intralayer $X$-$X$ hopping between the atoms in top and bottom layers. The hopping vectors are shown in Fig. 1(b). The additional vectors ($c_i$), beyond the six-band TBM, representing the hopping between the second-nearest-neighbor same-type atom are defined as follows:

$$\vec{c}_1 = \left(\frac{3}{2}a, \frac{\sqrt{3}}{2}a, 0\right), \quad \vec{c}_2 = (0, \sqrt{3}a, 0),$$

$$\vec{c}_3 = \left(-\frac{3}{2}a, \frac{\sqrt{3}}{2}a, 0\right), \quad \vec{c}_4 = \left(-\frac{3}{2}a, -\frac{\sqrt{3}}{2}a, 0\right),$$

$$\vec{c}_5 = (0, -\sqrt{3}a, 0), \quad \vec{c}_6 = \left(\frac{3}{2}a, -\frac{\sqrt{3}}{2}a, 0\right). \tag{11}$$

By further introducing the SOC and assuming that those interactions only exist in intra-atomic states, only the intra-atomic Hamiltonian matrix elements will be modulated. In general, the SOC in the TMDC monolayer can be described by

$$\mathcal{H}_{\mathrm{SOC}} = \sum_{\alpha} \frac{\lambda}{\hbar} \vec{L}_\alpha \cdot \vec{S}_\alpha, \tag{12}$$

where $\lambda_\alpha$ is the SOC strength related to different atom types, in this case, $\lambda_M$ and $\lambda_X$. The $\vec{L}_\alpha$ and $\vec{S}_\alpha$ are the orbital angular momentum operator and electronic spin operator. Following the abovementioned description and considering the parity of the basis function, the basis can be divided into even and odd parts. Hence, when introducing the SOC effect into the Hamiltonian, the whole Hamiltonian will consist of four parts by considering the basis function parity and the spin degree of freedom simultaneously, namely, (Even, ↑), (Even, ↓), (Odd, ↑), and (Odd, ↓). Finally, the Hamiltonian will be described by a $22 \times 22$ matrix, which is given by

$$\mathcal{H} = \begin{pmatrix} \mathcal{H}_{\mathrm{TB}} & 0 \\ 0 & \mathcal{H}_{\mathrm{TB}} \end{pmatrix} + \begin{pmatrix} \mathcal{H}_{\mathrm{SO}}^{\uparrow\uparrow} & \mathcal{H}_{\mathrm{SO}}^{\uparrow\downarrow} \\ \mathcal{H}_{\mathrm{SO}}^{\downarrow\uparrow} & \mathcal{H}_{\mathrm{SO}}^{\downarrow\downarrow} \end{pmatrix}, \tag{13}$$

where

$$\mathcal{H}_{\mathrm{SO}}^{\uparrow\uparrow} = \begin{pmatrix} \mathcal{H}_{\mathrm{SO1}}^{\uparrow\uparrow} & 0 \\ 0 & \mathcal{H}_{\mathrm{SO2}}^{\uparrow\uparrow} \end{pmatrix}, \quad \mathcal{H}_{\mathrm{SO}}^{\uparrow\downarrow} = \begin{pmatrix} 0 & \mathcal{H}_{\mathrm{SO1}}^{\uparrow\downarrow} \\ \mathcal{H}_{\mathrm{SO2}}^{\uparrow\downarrow} & 0 \end{pmatrix},$$

$$\mathcal{H}_{\mathrm{SO}}^{\downarrow\uparrow} = \begin{pmatrix} 0 & \mathcal{H}_{\mathrm{SO1}}^{\downarrow\uparrow} \\ \mathcal{H}_{\mathrm{SO2}}^{\downarrow\uparrow} & 0 \end{pmatrix}, \quad \mathcal{H}_{\mathrm{SO}}^{\downarrow\downarrow} = \begin{pmatrix} \mathcal{H}_{\mathrm{SO1}}^{\downarrow\downarrow} & 0 \\ 0 & \mathcal{H}_{\mathrm{SO2}}^{\downarrow\downarrow} \end{pmatrix}. \tag{14}$$

The detail on the SOC term can be found in Ref. [12] or Appendix B.

### E. Strain-dependent interatomic hopping parameters and on-site parameters

In the Slater-Koster TBM, the interatomic hopping parameters are two-center integrals representing the atomic orbital overlap [9]. Figure 1(c) shows that the atomic orbital overlap varies with strain. Thus, the effect of strain on the band structure may be modeled by applying interatomic-distance-dependent hopping parameters. Specifically, the hopping parameters under the lattice deformation are [18,32]

$$t_{ij,\mu\nu}(\vec{r_{ij}}) = t_{ij,\mu\nu}(\vec{r_{ij}^0})\left(1 - \Lambda_{ij,\mu\nu}\frac{|\vec{r}_{ij} - \vec{r}_{ij}^0|}{\vec{r}_{ij}^0}\right), \tag{15}$$

where $\vec{r}_{ij}^0$ and $\vec{r_{ij}}$ are the distance between atom $(i,\mu)$ and atom $(j,\nu)$ in the unstrained and strained TMDCs, respectively. The coefficient $\Lambda_{ij,\mu\nu}$ defined by $-d\ln t_{ij,\mu\nu}(r)/d\ln(r)|_{r=|r_{ij}^0|}$ characterizes the electron-phonon coupling strength of the corresponding bond [32], determined by directly comparing the shift of electrons levels with lattice deformation obtained by frozen-phonon DFT and coefficient $\Lambda_{ij,\mu\nu}$ obtained from the corresponding TBM. This method has been verified in bilayer graphene [33]; however, the large number of orbitals involved in the TBM of TMDCs hinders its application in TMDCs. To address this issue and derive the monolayer TMDC coefficients $\Lambda_{ij,\mu\nu}$, we

introduce the Wills-Harrison approach [34]:

$$t_{ij,\mu\nu}(r) \propto |r|^{-(l_\mu + l_\nu + 1)}, \tag{16}$$

where $l_\mu$, $l_\nu$ are the absolute value of the angular momentum for orbital $\mu$, $\nu$. In TMDCs, $l_d = 2$ and $l_p = 1$, so the coefficient $\Lambda$ for $p$-$p$ ($V_{pp\sigma}, V_{pp\pi}$), $p$-$d$ ($V_{pd\sigma}, V_{pd\pi}$), and $d$-$d$ ($V_{dd\sigma}, V_{dd\pi}, V_{dd\delta}$) should be 3, 4, and 5, respectively.

The pioneering work of Tserbak [35] and Boykin [36] demonstrated that the shifts in the diagonal Hamiltonian matrix elements (on-site parameters related to the crystal field) are also required for strained semiconductors. The on-diagonal parameters $\Delta_i$ are fitted to shift in proportion to the magnitude of the strain [35,36]:

$$\Delta_i = \Delta_{i0} + b_i(\varepsilon_\parallel - \varepsilon_\perp), \tag{17}$$

where $\varepsilon_\parallel$ and $\varepsilon_\perp$ are strain components parallel and perpendicular to the atom layer, $\Delta_{i0}$ are the on-site parameters for the unstrained materials, and $b_i$ is an orbital-dependent parameter that weigh the shifts with strain. This theoretical model worked well in some strained semiconductors such as Si, Ge [37], and GaAs [38]. We follow the above approach to derive the strain-dependent on-site parameters in TMDC monolayers.

## III. RESULT AND DISCUSSION

### A. Slater-Koster parameters of the six-band TBM

The six-band TBM introduced in Sec. II reproduces the band structures of monolayer $MoS_2$ and $WS_2$ when we choose an appropriate set of Slater-Koster parameters by fitting the energy level and energy dispersion of the high-symmetry points of CBs and VBs. Among them, we focus on the minimum of the CB located at the $K$ and/or $Q$ points and the maximum of the VB at the $K$ and/or $\Gamma$ points; these determined the band gap type and magnitude. Therefore, we sacrifice the accuracy of less important regions of the band structure to achieve the best accuracy for those near-gap points ($K$, $\Gamma$, and $Q$ points). The spin-orbit constants for transition metal $\lambda_M$ and chalcogens $\lambda_X$ are obtained by comparison with the spin-orbit splitting at the $K$ point obtained from DFT [11]. An appropriate set of Slater-Koster parameters and corresponding shift coefficients is listed in Tables II and III.

### B. Band structures of unstrained monolayer TMDCs by the six-band TBM

TBM band structures for monolayer $MoS_2$ and $WS_2$ are shown in Fig. 3 obtained using the DFT band structure-fitted Slater-Koster parameters listed in Table II. While the nearest- and/or next-nearest-neighbor hopping TBM does not capture all of the details of the DFT band structure, the TBM provides an excellent description of the VB edges at the $K$ and $\Gamma$ points and the CB edges at the $K$ and $Q$ points—these are sensitive to strain and determine how the band gap varies with strain. Thus, an accurate description of those points suffices to characterize the main strain effects on the relevant features of the band structure. Both the DFT (black dots) and TBM results (red solid lines) illustrate that monolayer $MoS_2$ has a direct band gap at the $K$ valley and the secondary minimum of the CB at the $Q$ point, where the latter possesses much higher

TABLE II. Slater-Koster parameters and SOC parameters. All parameters are in eV.

| | Label | $MoS_2$ | $WS_2$ |
|---|---|---|---|
| Crystal fields | $\Delta_0$ | −1.094 | −1.090 |
| | $\Delta_2$ | −1.511 | −1.525 |
| | $\Delta_p$ | −3.559 | −3.599 |
| | $\Delta_z$ | −6.886 | −7.598 |
| $M$-$X$ | $V_{pd\sigma}$ | −3.679 | −3.785 |
| | $V_{pd\pi}$ | 1.199 | 1.275 |
| $M$-$M$ | $V_{dd\sigma}$ | −0.895 | −0.925 |
| | $V_{dd\pi}$ | 0.252 | 0.261 |
| | $V_{dd\delta}$ | 0.228 | 0.220 |
| $X$-$X$ | $V_{pp\sigma}$ | 1.225 | 1.250 |
| | $V_{pp\pi}$ | −0.467 | −0.476 |
| SOC | $\lambda_M$ | 0.074 | 0.210 |
| | $\lambda_X$ | 0.052 | 0.159 |

TABLE III. Shift coefficient for the interatomic hopping and on-site terms. Note that, for $\Lambda_{d-d}$ for $V_{dd\delta}$, the sign of this term is −, which is different from the others. The sign of hopping parameters is determined by the bond type ($\sigma$, $\delta$, or $\pi$ bond). In general, $V_{dd\sigma} < 0$, $V_{dd\delta} < 0$, and $V_{dd\pi} > 0$ [39,40]. However, due to the difficulty to acquire the perfect set of parameters, the $V_{dd\delta}$ used in our model is >0. Therefore, we set the shift coefficient of $V_{dd\delta}$ as −5 rather than 5. All $b_i$ data are in eV.

| | Label | $MoS_2$ | $WS_2$ |
|---|---|---|---|
| Interatomic | $\Lambda_{p-p}$ | 3 | 3 |
| | $\Lambda_{p-d}$ | 4 | 4 |
| | $\Lambda_{d-d}$ | 5(−5 for $V_{dd\sigma}$) | 5(−5 for $V_{dd\sigma}$) |
| On-site | $b_0$ | 0.1 | 1.36 |
| | $b_2$ | −0.2 | −3.43 |
| | $b_p$ | −4.4 | −32.39 |
| | $b_z$ | 8.8 | 132.76 |

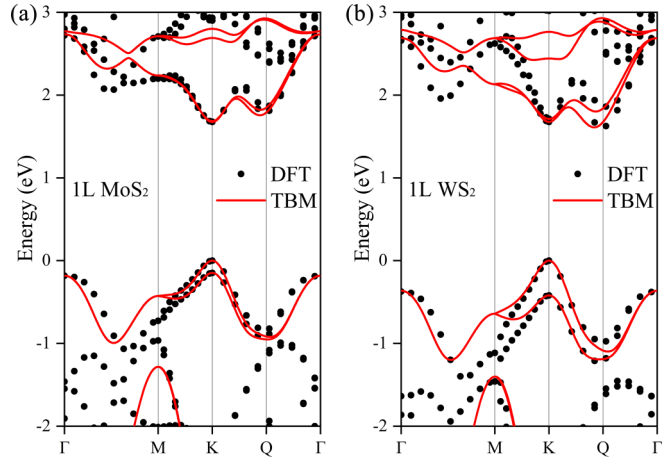


FIG. 3. Band structures of an unstrained (a) $MoS_2$ monolayer and (b) $WS_2$ monolayer obtained by density functional theory (DFT) and the six-band tight-binding model (TBM). Red solid lines (black dots) correspond to TBM (DFT) results. Noticeably, the energy of the maximum of the valance band (VB) is set to zero.

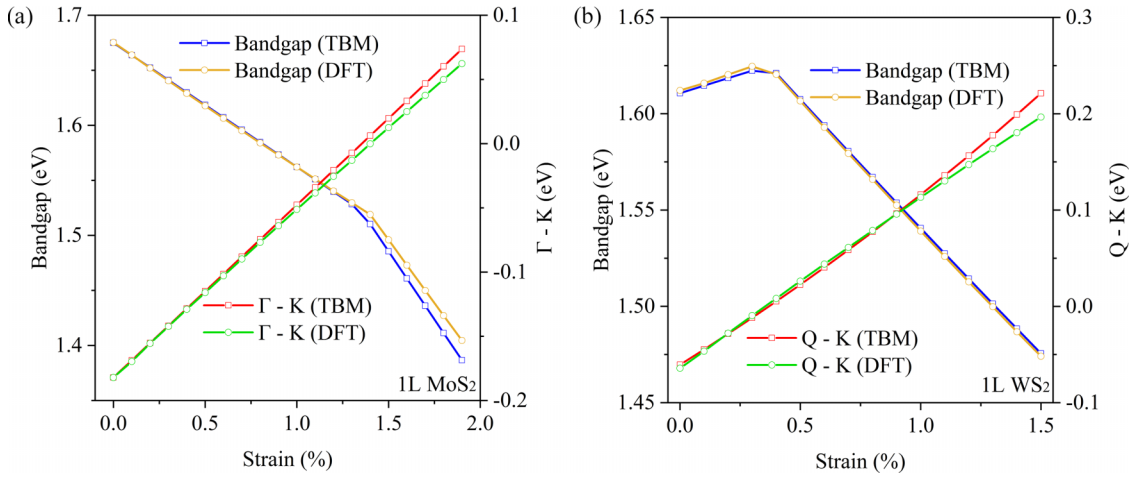


FIG. 4. Variation of the band gap and energy differences for special $k$ points with biaxial strain for (a) $MoS_2$ monolayer and (b) $WS_2$ monolayer obtained by the six-band tight-binding model (TBM). The direct-indirect band gap transition occurs at 1.4% biaxial strain in $MoS_2$ monolayer, and the indirect-direct band gap transition occurs at 0.4% biaxial strain in $WS_2$ monolayer.

energy (∼120 meV) than the $K$ point [see Fig. 3(a)]. However, monolayer $WS_2$ exhibits the indirect band gap ($Q$ to $K$) with the minimum of the CB at the $Q$ point [see Fig. 3(b)], which differs from the common sense that unstrained monolayer TMDCs are direct band gap semiconductors [22,23,41,42]. We attribute this discrepancy to differences in DFT algorithms (or possibly to differences in lattice constants employed in the DFT literature). On the other hand, Ahn *et al.* [43] experimentally imply that the intrinsic $WX_2$ monolayer is an indirect band gap semiconductor below room temperature, which leads to the observed abnormal enhancement of photoluminescence with increasing temperature.

### C. Band gap shift, Γ-point shift, and $Q$-point shift of the six-band TBM

Using the TBM parameters listed in Tables II and III, we determine how the band gap and strain energy difference of special $k$ points vary with strain. We focus on the energy difference between the VB Γ and $K$ points in $MoS_2$ and the energy difference between the CB $Q$ and $K$ points in $WS_2$—see Fig. 4. For the $MoS_2$ monolayer, the band gap decreases with increasing tensile biaxial strain (both DFT and TBM); the shift coefficients (derivative of the band gap with respect to biaxial strain) are nearly equivalent (−113.1 meV/% for DFT results and −112.8 meV/% for TBM results). The Γ-$K$ energy difference is zero at a biaxial strain of 1.4% for both DFT and TBM, as shown in Fig. 4(a); this corresponds to the direct-to-indirect band gap transition. The $WS_2$ monolayer exhibits an indirect band gap for biaxial strains between 0 and 0.4% (from the VB $K$ to the CB $Q$ points), as shown in Fig. 4(b). In the indirect band gap region, the band gap increases with increasing biaxial tensile strain due to the increasing energy of the CB $Q$ point. On the other hand, in the direct band gap region (>0.4% strain), the band gap decreases linearly with increasing biaxial tensile strain with a shift coefficient of −133.4 (−134.5) meV/% for TBM (DFT). Thus, the TBM demonstrates linear band gap shifts with strain as well as transitions between direct and indirect band gaps.

### D. Band structures of strained monolayer TMDCs by the six-band TBM

We next consider how well the TBM describes the band structure of strained TMDC monolayers, especially at the special points (Γ, $K$, and $Q$). We use the parameters listed in Tables II and III to calculate the band structures of the $MoS_2$ monolayer under 1.5% biaxial strain and the $WS_2$ monolayer under 0.7% biaxial strain; see Figs. 5(a) and 5(b). The TBM qualitatively reproduces the overall DFT band structure and is quantitative at the high-symmetry points. However, there are situations in which the quantitative agreement is less than ideal, e.g., the CB $Q$ point in $MoS_2$ and the VB Γ point in $WS_2$. These points were not included in fitting the shift parameters (these focused upon the VB Γ point in $MoS_2$ and the CB $Q$ point in $WS_2$). In $WS_2$, large on-site shift coefficients

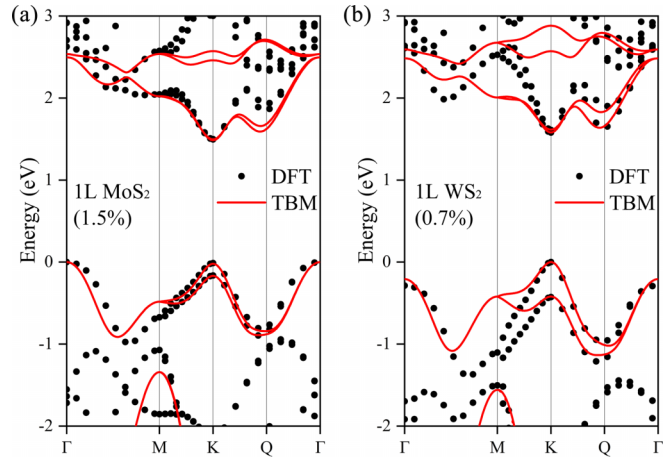


FIG. 5. Band structures of an strained $MoS_2$ monolayer and $WS_2$ monolayer obtained by density functional theory (DFT) and the six-band tight-binding model (TBM). (a) Band structure of $MoS_2$ monolayer under 1.5% biaxial strain. (b) Band structure of $WS_2$ monolayer under 0.7% biaxial strain. Red solid lines correspond to TBM results, and black dots correspond to DFT results. The maximum valence band (VB) energy was set to zero.

TABLE IV. Slater-Koster parameters and SOC parameters used in the 11-band TBM. All Slater-Koster parameters and $b$ are in eV.

| | Label | $MoS_2$($\Lambda$ or $b$) | $WS_2$($\Lambda$ or $b$) |
|---|---|---|---|
| Even part | $E^e_{d0}$ | −0.5048 (−2.692) | −0.3429 (−3.429) |
| | $E^e_{d1}$ | −0.2399 (1.167) | −0.8690 (9.732) |
| | $E^e_{s1}$ | −4.5896 (−70.28) | −4.6903 (−70.04) |
| | $E^e_{s2}$ | −9.352 (−124.7) | −10.718 (−142.9) |
| | $V^e_{pd\pi}$ | −1.4399 (+4) | −1.4058 (+4) |
| | $V^e_{pd\sigma}$ | 4.9182 (+4) | 6.1212 (+4) |
| | $V^e_{pp\sigma}$ | −0.1024 (+3) | −0.4416 (+3) |
| | $V^e_{pp\pi}$ | −0.5173 (−3) | −0.4557 (−3) |
| | $V^e_{dd\sigma}$ | −0.8060 (−5) | −1.0730 (−5) |
| | $V^e_{dd\pi}$ | 0.6847 (−5) | 0.8816 (−5) |
| | $V^e_{dd\delta}$ | 0.3275 (+5) | 0.41004 (+5) |
| | $K^e_{pp\sigma}$ | 0.4170 (−3) | 0.1585 (−3) |
| | $K^e_{pp\pi}$ | 0.0016 (+3) | 0.0292 (+3) |
| | $K^e_{dd\sigma}$ | 0.0377 (+5) | 0.0609 (+5) |
| | $K^e_{dd\pi}$ | 0.1153 (−5) | 0.1534 (−5) |
| | $K^e_{dd\delta}$ | −0.0366 (−5) | −0.0109 (−5) |
| | | $MoS_2$($\Lambda$ or $b$) | $WS_2$($\Lambda$ or $b$) |
| Odd part | $E^o_{d2}$ | 0.5624 (3.7493) | 0.9765 (13.02) |
| | $E^o_{s1}$ | −1.525 (−10.16) | −0.9087 (−12.12) |
| | $E^o_{s2}$ | −0.6737 (−4.491) | −1.0191 (−13.59) |
| | $V^o_{pd\pi}$ | −0.8832 (+4) | −0.9413 (+4) |
| | $V^o_{pd\sigma}$ | 2.5811 (+4) | 2.7891 (+4) |
| | $V^o_{pp\sigma}$ | 0.9107 (−3) | 0.9425 (−3) |
| | $V^o_{pp\pi}$ | −0.3095 (−3) | −0.2980 (−3) |
| | $V^o_{dd\sigma}$ | −1.0740 (−5) | −1.0740 (−5) |
| | $V^o_{dd\pi}$ | 0.0180 (−5) | −0.0170 (+5) |
| | $V^o_{dd\delta}$ | 0.0596 (+5) | 0.00432 (+5) |
| | $K^o_{pp\sigma}$ | −0.0442 (+3) | −0.0189 (+3) |
| | $K^o_{pp\pi}$ | 0.0103 (+3) | 0.0293 (+3) |
| | $K^o_{dd\sigma}$ | 0.0012 (−5) | 0.0012 (−5) |
| | $K^o_{dd\pi}$ | 0.0061 (−5) | −0.0162 (+5) |
| | $K^o_{dd\delta}$ | 0.0221 (+5) | −0.0229 (−5) |
| | | $MoS_2$ | $WS_2$ |
| SOC | $\lambda_M$ | 0.1050 | 0.3188 |
| | $\lambda_X$ | 0.0536 | 0.0536 |

were necessary to reproduce the variation of the CB $Q$ point but led to an overestimate of the strain effect on the VB Γ point. Accordingly, we sacrificed the accuracy of the $Q$ point to obtain good fit with respect to the Γ point in the $MoS_2$ monolayer. Despite these limitations, the TBMs do provide reasonable descriptions of the main features of how the band structure changes with strain.

We note that it is possible to obtain TBM coefficients and shift coefficients that give superior overall fits to the DFT band structure by including more data in the training set, especially data for other points in the band structure and by going to larger strain. The choice depends on which features of the band structure are important for the applications of interest. Here, our focus was on how strain modifies the band structure points that determine whether the band gaps are direct or indirect. By the way, we can seek a more accurate model which contains more Slater-Koster parameters that may better describe the band structure and its evolution with strain. To verify the above illustration and conjecture, in the next section, we use the 11-band TBM determined by 31 Slater-Koster parameters to fit the results obtained by DFT-HSE calculation.

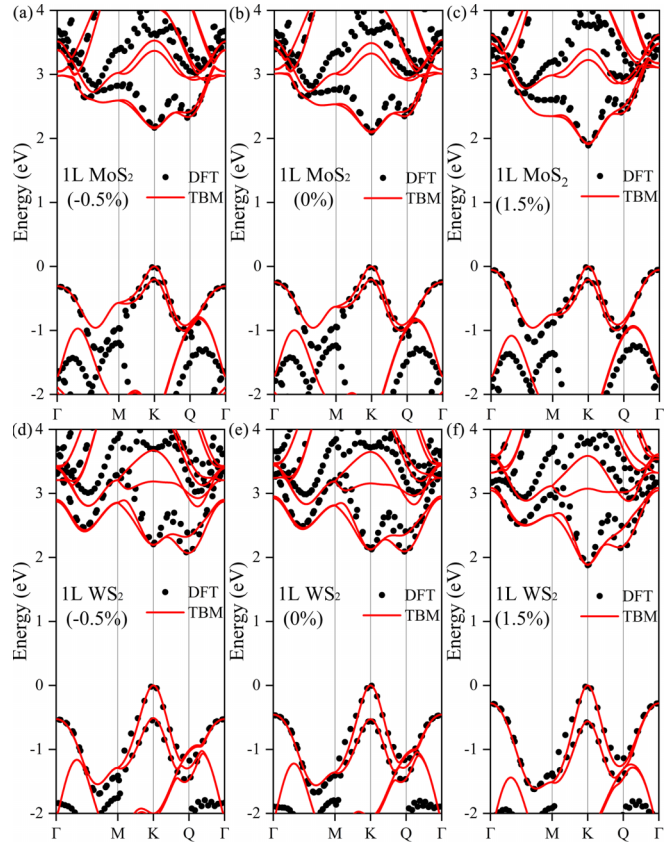


FIG. 6. Band structure of monolayer (a)–(c) $MoS_2$ and (d)–(f) $WS_2$ under different strain level. The black dots and red solid lines represent the results obtained by DFT-HSE and the 11-band tight-binding model (TBM), respectively.

### E. Band structures of monolayer TMDCs by the 11-band TBM and DFT-HSE

To demonstrate that our abovementioned effects of strain on TB parameters are reliable and generalizable. We extend the above method to 11-band TBM and DFT-HSE calculations. The 11-band TBM considers more bands, which needs more TB parameters to describe the Hamiltonian and subsequently the band structure. We use the same method as discussed in Sec III A to fit the calculation results using VASP with the HSE hybrid function approach [44]. The Slater-Koster parameters used in the 11-band TBM are given in Table IV. To make the 11-band TBM results under strain consistent with the HSE results, we follow the discussion in the caption of Table III to select the appropriate shift coefficient parameters ($\Lambda$ or $b$) for the interatomic hopping term and on-site term, shown in Table IV. We display in Fig. 6 the evolution process of band structure with strain level obtained by both HSE results and the 11-band TBM. In this section, we further study the band structure under compressive strain, and the strain range is from −0.5 to 1.5%. We can see that the TBM results predict the well-fitted band structure of monolayer TMDCs under different strain levels, especially at some special points, such as $K$, $Q$, $M$, and Γ points.

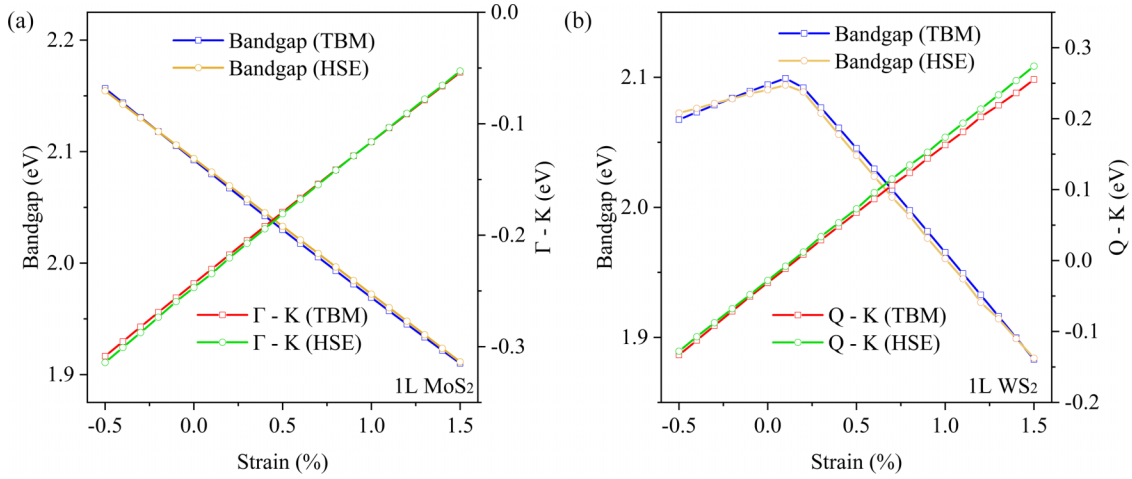


FIG. 7. Variation of the band gap and energy differences for special $k$ points with biaxial strain for (a) $MoS_2$ monolayer and (b) $WS_2$ monolayer obtained by the 11-band tight-binding model (TBM). The indirect-direct band gap transition occurs at 0.2% biaxial strain in $WS_2$ monolayer.

### F. Band gap shift, Γ-point shift, and $Q$-point shift of the 11-band TBM

Following a similar discussion in Sec. III C, we focus on the energy difference between the VB Γ and $K$ points in $MoS_2$ and the energy difference between the CB $Q$ and $K$ points in $WS_2$. Using the TBM parameters listed in Table IV, we determine the band gap and strain energy difference of special $k$ points under different strain levels, as displayed in Fig. 7. The $WS_2$ monolayer also shows indirect-to-direct band gap transition when we change the DFT calculations to DFT-HSE calculations. The TBM results of the band gap, energy shift of high-symmetry points ($Q$, $K$, and Γ) are consistent with that of the HSE results. These results further demonstrate that our proposed strain-related shift-coefficient-parameter-mediated TBM for strained TMDC monolayers can well describe the evolution of their band structure at different strain levels, and this method is universal, achieving good agreement in different TBM (6- or 11-band) and the use of the first-principles calculation methods (DFT-PBE or DFT-HSE).

### G. Strain-induced changing of electron effective mass and SOC splitting by the 11-band TBM

After confirming the feasibility of our strain-related TBM, we can also simply calculate other electrical properties of monolayer TMDCs that are potentially modulated by external strain, such as SOC splitting and effective mass of electrons. From Fig. 8, it is evident that the SOC splitting is significantly influenced by strain, which may be surprising. After all, SOC is primarily a relativistic effect inherent to atomic cores, making it primarily an atomic property. However, as the strain increases, the SOC in the VB progressively increases, maintaining consistency across both compressive and tensile strains. For $MoS_2(WS_2)$, the change in the SOC splitting value is $\sim$2 (25) meV/%. Our interpretation is that, while strain does not alter the intrinsic properties of atoms, it does influence the intermixing of various atomic orbitals (for instance, different $M$ atom $d$ and $X$ $p$ orbitals), thus significantly affecting the effective spin-orbit splitting. This finding aligns with previous research trends [45], yet our observed change

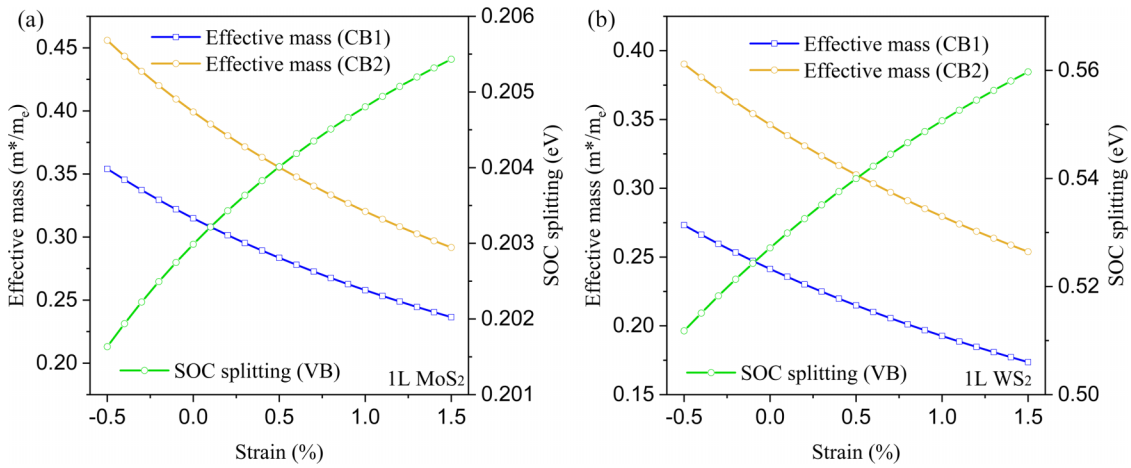


FIG. 8. Effective mass of electron at $K(K')$ valley and spin-orbit coupling (SOC) splitting value of valence band (VB) $K$ points for (a) monolayer $MoS_2$ and (b) monolayer $WS_2$ obtained by the 11-band tight-binding model (TBM).

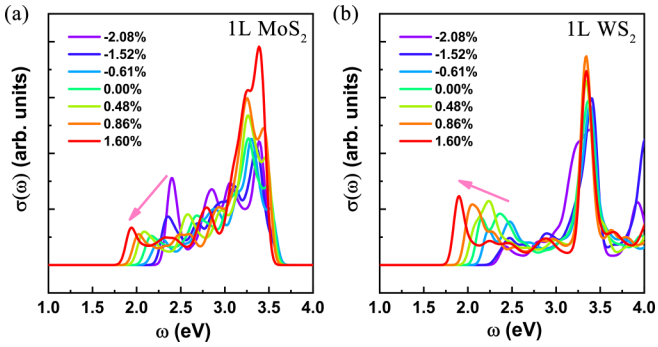


FIG. 9. Optical conductivity of monolayer (a) $MoS_2$ and (b) $WS_2$ under different strain level. The pink arrow indicates the increasing trend of the A exciton peak with increasing tensile strain.

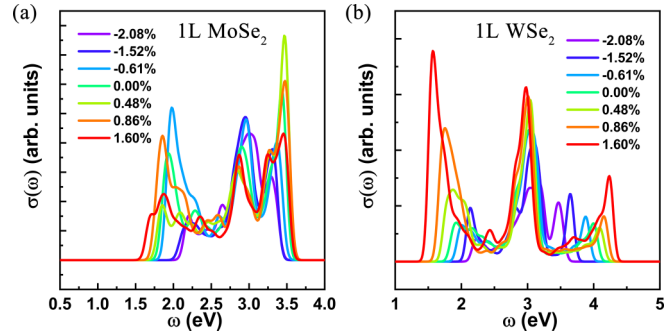


FIG. 10. Optical conductivity of monolayer (a) $MoSe_2$ and (b) $WSe_2$ under different strain level.

in SOC splitting with strain is roughly twice that reported in those studies. This discrepancy likely arises from the biaxial strain applied in our study, as opposed to the uniaxial strain reported in Ref. [45].

Furthermore, as shown in Fig. 8, we calculate the effective mass of electrons located at $K$ points following the formula:

$$m^* = \frac{\hbar^2}{d^2E/dk^2}. \tag{18}$$

Due to the SOC effect, the electrons in different CBs have different effective masses. We can also observe that, as strain increases, the effective masses of electrons in both CBs tend to decrease. Typically, a smaller effective mass of electrons is associated with higher carrier mobility, potentially enhancing the performance of electronic devices. This information can inform simulations of these materials in fields such as electronic design automation.

### H. Optical conductivity of strained monolayer TMDCs by the 11-band TBM

Once we have developed the TBM for TMDCs under strain, we can utilize it to calculate and predict some strain-level-dependent observables, such as the optical conductivity $\sigma(\omega)$. For this purpose, we employ the Kubo formula:

$$\begin{aligned}\sigma(\omega) = \frac{e^2}{h}\frac{\hbar}{A\omega}\sum_{mn,\mathbf{k}}&[f(E_n) - f(E_m)]\\ &\times|\langle\Psi_n(\mathbf{k})|\widehat{v}|\Psi_m(\mathbf{k})\rangle|^2\\ &\times\delta\{\hbar\omega - [E_n(\mathbf{k}) - E_m(\mathbf{k})]\},\end{aligned} \tag{19}$$

to calculate it, where $A$ is the constant representing the unit cell area, $\Psi_n(\mathbf{k})$ is the eigenstate of eigenenergy $E_n$, $f(E_n)$ is the Fermi-Dirac distribution function, and $\widehat{v} = (1/\hbar)\partial\widehat{H}/\partial\mathbf{k}$ is the velocity operator. As illustrated in Figs. 9 and 10, we observe that, for all materials, there is a threshold for the optical transitions, which nearly equals the energy gap. For the first peak, it splits into two peaks due to the SOC effect, resulting in the emergence of two groups of optical transitions in the spectrum. Given that the SOC of heavier W atoms is stronger, this effect is particularly pronounced in $WX_2$ materials, where these two peaks align with the absorption peaks of A and B excitons in the optical absorption spectrum. In the higher-energy region, we identify a primary peak, which is attributed to band-nesting effects and corresponds to the C exciton peak in the absorption spectrum. Next, we examine how these optical conductivities vary under strain in $MoS_2$ and $WS_2$. We observe that, for both materials, as strain increases, their first peak experiences a redshift, aligning with the redshift observed in our band calculations. However, the difference lies in the fact that, with the increase in strain for $MoS_2$, the absolute value of the peak tends to decrease (especially when compared with the value of the C exciton peak), whereas for $WS_2$, the trend is reversed, with the absolute value of the peak increasing as strain increases (as indicated by the pink arrows in the figure). This phenomenon can be reflected by the changes in the band structure under strain. For $MoS_2$, as strain increases, the energy of the $\Gamma$ point and $K$ on the VB approach each other, indicating a trend toward transitioning from a direct to an indirect band gap. For the $WS_2$ monolayer, as strain increases, it transitions from an indirect to a direct band gap, leading to an increase in optical conductivity with increasing strain. The same phenomenon is observed in $WSe_2$. This theoretical prediction aligns with experimental findings. For $MoS_2$, as strain increases, the photoluminescence (PL) of monolayer $MoS_2$ weakens [46]. Conversely, for $WX_2$ materials, their PL or absorption significantly increases [47,48], which further confirms the effectiveness of our modified model.

## IV. CONCLUSIONS

In conclusion, we have applied the Slater-Koster TBM approach to investigate strain effects on the band structures of monolayer $MoS_2$ and $WS_2$ by accounting for how the relevant TBM parameters vary with strain. We found that those Slater-Koster parameters representing orbital overlap provide information on how the parameters associated with the hopping processes vary with strain and the sign of the shifts of these parameters with respect to strain. This approach enables the construction of a more precise TBM for describing the influence of strain on the electron hopping processes and on-site energies. Our TBM can determine both strain-dependent shifts in the band gap and the energies of the bands at high-symmetry $k$ points. Therefore, we believe that this theory has the potential to be extended to other systems that can be described using the TBM and TBM parameters, such as defect

states caused by atomic vacancies in TMDC monolayers [49]. Overall, the agreement with DFT calculations for these critical features of the band structure will provide a valuable approach for investigating more complex strain states and local variations in strain in general 2D materials or even some confined finite systems with low symmetry.

## ACKNOWLEDGMENTS

We are grateful to Yuanyuan Wang for enlightening discussions. We gratefully acknowledge the financial support by the RGC of Hong Kong (ZP, HW, and DL—GRF Grant No. 15304519, DJS and GZ—GRF Grant No. 11211019).

## APPENDIX A: FULL DESCRIPTION OF TERMS IN THE HAMILTONIAN OF TMDC MONOLAYERS OF THE SIX-BAND TBM

The full description of the terms in the Hamiltonian in Eq. (4) will be discussed in this Appendix. According to Ref. [11], Eq. (4) can be illustrated in a compact form:

$$\Delta = \begin{pmatrix} \Delta_M & 0 \\ 0 & \Delta_X \end{pmatrix}, \tag{A1}$$

where

$$\Delta_M = \begin{pmatrix} \Delta_0 & 0 & 0 \\ 0 & \Delta_2 & -i\lambda_M \hat{s}_z \\ 0 & i\lambda_M \hat{s}_z & \Delta_2 \end{pmatrix}, \tag{A2}$$

$$\Delta_X = \begin{pmatrix} \Delta_p + t_{xx}^{\perp} & -i\frac{\lambda_X}{2}\hat{s}_z & 0 \\ -i\frac{\lambda_X}{2}\hat{s}_z & \Delta_p + t_{yy}^{\perp} & 0 \\ 0 & 0 & \Delta_z - t_{zz}^{\perp} \end{pmatrix}, \tag{A3}$$

where $t_{xx}^{\perp} = t_{yy}^{\perp} = V_{pp\pi}$, $t_{zz}^{\perp} = V_{pp\sigma}$, and those terms are expected to represent the effect of hopping in the vertical direction between top and bottom $X$ atoms. Here, $\lambda_M$ and $\lambda_X$ are the SOC of the $M$ and $X$ atoms, respectively. The hopping effect between the nearest neighbors ($M$-$X$) are [18]

$$t_1^{MX} = \frac{\sqrt{2}}{7\sqrt{7}} \begin{pmatrix} -9V_{pd\pi} + \sqrt{3}V_{pd\sigma} & 3\sqrt{3}V_{pd\pi} - V_{pd\sigma} & 12V_{pd\pi} + \sqrt{3}V_{pd\sigma} \\ 5\sqrt{3}V_{pd\pi} + 3V_{pd\sigma} & 9V_{pd\pi} - \sqrt{3}V_{pd\sigma} & -2\sqrt{3}V_{pd\pi} + 3V_{pd\sigma} \\ -V_{pd\pi} - 3\sqrt{3}V_{pd\sigma} & 5\sqrt{3}V_{pd\pi} + 3V_{pd\sigma} & 6V_{pd\pi} - 3\sqrt{3}V_{pd\sigma} \end{pmatrix}, \tag{A4}$$

$$t_2^{MX} = \frac{\sqrt{2}}{7\sqrt{7}} \begin{pmatrix} 0 & -6\sqrt{3}V_{pd\pi} + 2V_{pd\sigma} & 12V_{pd\pi} + \sqrt{3}V_{pd\sigma} \\ 0 & -6V_{pd\pi} - 4\sqrt{3}V_{pd\sigma} & 4\sqrt{3}V_{pd\pi} - 6V_{pd\sigma} \\ 14V_{pd\pi} & 0 & 0 \end{pmatrix}, \tag{A5}$$

$$t_3^{MX} = \frac{\sqrt{2}}{7\sqrt{7}} \begin{pmatrix} 9V_{pd\pi} - \sqrt{3}V_{pd\sigma} & 3\sqrt{3}V_{pd\pi} - V_{pd\sigma} & 12V_{pd\pi} + \sqrt{3}V_{pd\sigma} \\ -5\sqrt{3}V_{pd\pi} - 3V_{pd\sigma} & 9V_{pd\pi} - \sqrt{3}V_{pd\sigma} & -2\sqrt{3}V_{pd\pi} + 3V_{pd\sigma} \\ -V_{pd\pi} - 3\sqrt{3}V_{pd\sigma} & -5\sqrt{3}V_{pd\pi} - 3V_{pd\sigma} & -6V_{pd\pi} + 3\sqrt{3}V_{pd\sigma} \end{pmatrix}. \tag{A6}$$

The hopping effect between the nearest same kinds of atoms ($M$-$M$, $X$-$X$) are

$$t_1^{MM} = \frac{1}{4} \begin{bmatrix} 3V_{dd\delta} + V_{dd\sigma} & \frac{\sqrt{3}}{2}(-V_{dd\delta} + V_{dd\sigma}) & \frac{3}{2}(-V_{dd\delta} + V_{dd\sigma}) \\ \frac{\sqrt{3}}{2}(-V_{dd\delta} + V_{dd\sigma}) & \frac{1}{4}(V_{dd\delta} + 12V_{dd\pi} + 3V_{dd\sigma}) & \frac{\sqrt{3}}{4}(V_{dd\delta} - 4V_{dd\pi} + 3V_{dd\sigma}) \\ \frac{3}{2}(-V_{dd\delta} + V_{dd\sigma}) & \frac{\sqrt{3}}{4}(V_{dd\delta} - 4V_{dd\pi} + 3V_{dd\sigma}) & \frac{1}{4}(3V_{dd\delta} + 4V_{dd\pi} + 9V_{dd\sigma}) \end{bmatrix}, \tag{A7}$$

$$t_2^{MM} = \frac{1}{4} \begin{bmatrix} 3V_{dd\delta} + V_{dd\sigma} & \sqrt{3}(V_{dd\delta} - V_{dd\sigma}) & 0 \\ \sqrt{3}(V_{dd\delta} - V_{dd\sigma}) & V_{dd\delta} + 3V_{dd\sigma} & 0 \\ 0 & 0 & 4V_{dd\pi} \end{bmatrix}, \tag{A8}$$

$$t_3^{MM} = \frac{1}{4} \begin{bmatrix} 3V_{dd\delta} + V_{dd\sigma} & \frac{\sqrt{3}}{2}(-V_{dd\delta} + V_{dd\sigma}) & -\frac{3}{2}(-V_{dd\delta} + V_{dd\sigma}) \\ \frac{\sqrt{3}}{2}(-V_{dd\delta} + V_{dd\sigma}) & \frac{1}{4}(V_{dd\delta} + 12V_{dd\pi} + 3V_{dd\sigma}) & -\frac{\sqrt{3}}{4}(V_{dd\delta} - 4V_{dd\pi} + 3V_{dd\sigma}) \\ -\frac{3}{2}(V_{dd\delta} - V_{dd\sigma}) & -\frac{\sqrt{3}}{4}(V_{dd\delta} - 4V_{dd\pi} + 3V_{dd\sigma}) & \frac{1}{4}(3V_{dd\delta} + 4V_{dd\pi} + 9V_{dd\sigma}) \end{bmatrix}, \tag{A9}$$

$$t_1^{XX} = \frac{1}{4} \begin{bmatrix} 3V_{pp\pi} + V_{pp\sigma} & \sqrt{3}(V_{pp\pi} - V_{pp\sigma}) & 0 \\ \sqrt{3}(V_{pp\pi} - V_{pp\sigma}) & V_{pp\pi} + 3V_{pp\sigma} & 0 \\ 0 & 0 & 4V_{pp\pi} \end{bmatrix}, \tag{A10}$$

$$t_2^{XX} = \begin{pmatrix} V_{pp\sigma} & 0 & 0 \\ 0 & V_{pp\pi} & 0 \\ 0 & 0 & V_{pp\pi} \end{pmatrix}, \tag{A11}$$

$$t_3^{XX} = \frac{1}{4} \begin{bmatrix} 3V_{pp\pi} + V_{pp\sigma} & -\sqrt{3}(V_{pp\pi} - V_{pp\sigma}) & 0 \\ -\sqrt{3}(V_{pp\pi} - V_{pp\sigma}) & V_{pp\pi} + 3V_{pp\sigma} & 0 \\ 0 & 0 & 4V_{pp\pi} \end{bmatrix}. \tag{A12}$$

The subindices 1, 2, and 3 represent the hopping direction shown in Fig. 1(b). From the above formulas, it is obvious that the TBM Hamiltonian can be described by 11 Slater-Koster parameters ($\Delta_0$, $\Delta_2$, $\Delta_p$, $\Delta_z$, $V_{pd\sigma}$, $V_{pd\pi}$, $V_{dd\sigma}$, $V_{dd\pi}$, $V_{dd\delta}$, $V_{pp\sigma}$, and $V_{pp\pi}$), which makes this TBM a semiempirical model and reduces the computational complexity.

## APPENDIX B: FULL DESCRIPTION OF THE SOC TERMS OF THE 11-BAND TBM

The full description of the SOC terms of Eq. (13) will be displayed in this Appendix and defined as

$$\mathcal{H}_{\mathrm{SO1}}^{\uparrow\uparrow} = \begin{pmatrix} 0 & 0 & 0 & 0 & 0 & 0 \\ 0 & 0 & i\lambda_M & 0 & 0 & 0 \\ 0 & -i\lambda_M & 0 & 0 & 0 & 0 \\ 0 & 0 & 0 & 0 & 0 & 0 \\ 0 & 0 & 0 & 0 & 0 & -\frac{i}{2}\lambda_X \\ 0 & 0 & 0 & 0 & \frac{i}{2}\lambda_X & 0 \end{pmatrix}, \quad \text{(B1)}$$

$$\mathcal{H}_{\mathrm{SO2}}^{\uparrow\uparrow} = \begin{pmatrix} 0 & -\frac{i}{2}\lambda_M & 0 & 0 & 0 & 0 \\ \frac{i}{2}\lambda_M & 0 & 0 & 0 & 0 & 0 \\ 0 & 0 & 0 & 0 & 0 & 0 \\ 0 & 0 & 0 & 0 & 0 & -\frac{i}{2}\lambda_X \\ 0 & 0 & 0 & 0 & \frac{i}{2}\lambda_X & 0 \end{pmatrix}, \quad \text{(B2)}$$

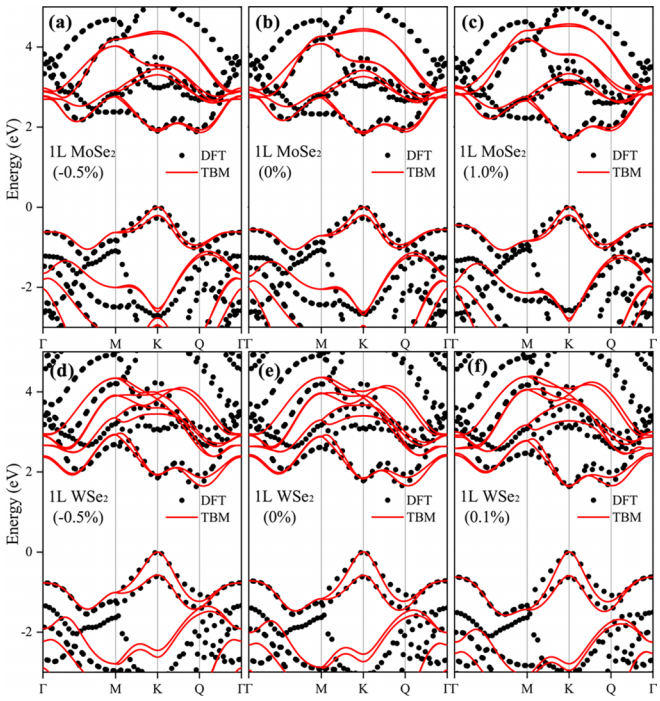


FIG. 11. Band structure of monolayer (a)–(c) $MoSe_2$ and (d)–(f) $WSe_2$ under different strain level. The black dots and red solid lines represent the results obtained by DFT-HSE and the 11-band tight-binding model (TBM), respectively.

$$\mathcal{H}_{\mathrm{SO1}}^{\uparrow\downarrow} = \begin{pmatrix} -\frac{\sqrt{3}}{2}\lambda_M & i\frac{\sqrt{3}}{2}\lambda_M & 0 & 0 & 0 \\ -i\frac{\lambda_M}{2} & \frac{\lambda_M}{2} & 0 & 0 & 0 \\ \frac{\lambda_M}{2} & i\frac{\lambda_M}{2} & 0 & 0 & 0 \\ 0 & 0 & 0 & -\frac{\lambda_X}{2} & i\frac{\lambda_X}{2} \\ 0 & 0 & \frac{\lambda_X}{2} & 0 & 0 \\ 0 & 0 & -i\frac{\lambda_X}{2} & 0 & 0 \end{pmatrix}, \quad \text{(B3)}$$

TABLE V. Slater-Koster parameters and SOC parameters used in the 11-band TBM for $WSe_2$ and $MoSe_2$. All Slater-Koster parameters and $b$ are in eV.

| | Label | $MoSe_2$($\Lambda$ or $b$) | $WSe_2$($\Lambda$ or $b$) |
|---|---|---|---|
| Even part | $E^e_{d0}$ | −0.2080 (−3.885) | −0.3799 (−3.770) |
| | $E^e_{d1}$ | −0.0840 (1.268) | −0.9623 (10.00) |
| | $E^e_{s1}$ | −4.2912 (−67.28) | −5.4430 (−81.23) |
| | $E^e_{s2}$ | −7.1074 (−104.7) | −7.987 (−135.5) |
| | $V^e_{pd\pi}$ | −1.2671 (+4) | −1.2484 (+4) |
| | $V^e_{pd\sigma}$ | 4.3280 (+4) | 5.4356 (+4) |
| | $V^e_{pp\sigma}$ | −0.0932 (+3) | −0.4045 (+3) |
| | $V^e_{pp\pi}$ | −0.5639 (−3) | −0.4940 (−3) |
| | $V^e_{dd\sigma}$ | −0.9269 (−5) | −1.2233 (−5) |
| | $V^e_{dd\pi}$ | 0.7874 (−5) | 1.0051 (−5) |
| | $V^e_{dd\delta}$ | 0.2784 (+5) | 0.3526 (+5) |
| | $K^e_{pp\sigma}$ | 0.3795 (−3) | 0.1718 (−3) |
| | $K^e_{pp\pi}$ | 0.0014 (+3) | 0.0268 (+3) |
| | $K^e_{dd\sigma}$ | 0.0320 (+5) | 0.0524 (+5) |
| | $K^e_{dd\pi}$ | 0.1326 (−5) | 0.1748 (−5) |
| | $K^e_{dd\delta}$ | −0.0421 (−5) | −0.0124 (−5) |
| | | $MoSe_2$($\Lambda$ or $b$) | $WSe_2$($\Lambda$ or $b$) |
| Odd part | $E^o_{d2}$ | 1.1248 (3.9456) | 0.5219 (6.510) |
| | $E^o_{s1}$ | −1.9826 (−8.16) | −1.6887 (−22.60) |
| | $E^o_{s2}$ | −0.7411 (−4.491) | −1.9386 (−13.59) |
| | $V^o_{pd\pi}$ | −0.7772 (+4) | −0.8359 (+4) |
| | $V^o_{pd\sigma}$ | 2.2714 (+4) | 2.4767 (+4) |
| | $V^o_{pp\sigma}$ | 0.9926 (−3) | 1.0216 (−3) |
| | $V^o_{pp\pi}$ | −0.3373 (−3) | −0.3231 (−3) |
| | $V^o_{dd\sigma}$ | −1.2351 (−5) | −1.2244 (−5) |
| | $V^o_{dd\pi}$ | 0.02070 (−5) | −0.0147 (+5) |
| | $V^o_{dd\delta}$ | 0.0507 (+5) | 0.0037 (+5) |
| | $K^o_{pp\sigma}$ | −0.0403 (+3) | −0.0173 (+3) |
| | $K^o_{pp\pi}$ | 0.0094 (+3) | 0.0269 (+3) |
| | $K^o_{dd\sigma}$ | 0.0014 (−5) | 0.0014 (−5) |
| | $K^o_{dd\pi}$ | 0.0070 (−5) | −0.0139 (+5) |
| | $K^o_{dd\delta}$ | 0.0188 (+5) | −0.0261 (−5) |
| | | $MoSe_2$ | $WSe_2$ |
| SOC | $\lambda_M$ | 0.1050 | 0.3188 |
| | $\lambda_X$ | 0.1680 | 0.1680 |

$$\mathcal{H}_{\mathrm{SO2}}^{\uparrow\downarrow}=\begin{pmatrix} \frac{\sqrt{3}}{2}\lambda_M & i\frac{\lambda_M}{2} & -\frac{\lambda_M}{2} & 0 & 0 & 0 \\ -i\frac{\sqrt{3}}{2}\lambda_M & -\frac{\lambda_M}{2} & -i\frac{\lambda_M}{2} & 0 & 0 & 0 \\ 0 & 0 & 0 & 0 & -\frac{\lambda_X}{2} & i\frac{\lambda_X}{2} \\ 0 & 0 & 0 & \frac{\lambda_X}{2} & 0 & 0 \\ 0 & 0 & 0 & -i\frac{\lambda_X}{2} & 0 & 0 \end{pmatrix}, \tag{B4}$$

$$\mathcal{H}_{\mathrm{SO1}}^{\downarrow\uparrow}=\begin{pmatrix} \frac{\sqrt{3}}{2}\lambda_M & i\frac{\sqrt{3}}{2}\lambda_M & 0 & 0 & 0 \\ -i\frac{\lambda_M}{2} & -\frac{\lambda_M}{2} & 0 & 0 & 0 \\ -\frac{3}{2}\lambda_M & -\frac{3}{2}\lambda_M & 0 & 0 & 0 \\ 0 & 0 & 0 & \frac{\lambda_X}{2} & i\frac{\lambda_X}{2} \\ 0 & 0 & -\frac{\lambda_X}{2} & 0 & 0 \\ 0 & 0 & -i\frac{\lambda_X}{2} & 0 & 0 \end{pmatrix}, \tag{B5}$$

$$\mathcal{H}_{\mathrm{SO2}}^{\downarrow\uparrow}=\begin{pmatrix} -\frac{\sqrt{3}}{2}\lambda_M & -i\frac{\lambda_M}{2} & \frac{\lambda_M}{2} & 0 & 0 & 0 \\ -i\frac{\sqrt{3}}{2}\lambda_M & \frac{\lambda_M}{2} & -i\frac{\lambda_M}{2} & 0 & 0 & 0 \\ 0 & 0 & 0 & 0 & \frac{\lambda_X}{2} & i\frac{\lambda_X}{2} \\ 0 & 0 & 0 & -i\frac{\lambda_X}{2} & 0 & 0 \\ 0 & 0 & 0 & -i\frac{\lambda_X}{2} & 0 & 0 \end{pmatrix}, \tag{B6}$$

$$\mathcal{H}_{\mathrm{SO1}}^{\downarrow\downarrow}=\begin{pmatrix} 0 & 0 & 0 & 0 & 0 & 0 \\ 0 & 0 & -i\lambda_M & 0 & 0 & 0 \\ 0 & i\lambda_M & 0 & 0 & 0 & 0 \\ 0 & 0 & 0 & 0 & 0 & 0 \\ 0 & 0 & 0 & 0 & 0 & \frac{i}{2}\lambda_X \\ 0 & 0 & 0 & 0 & -\frac{i}{2}\lambda_X & 0 \end{pmatrix}, \tag{B7}$$

$$\mathcal{H}_{\mathrm{SO1}}^{\downarrow\downarrow}=\begin{pmatrix} 0 & i\frac{\lambda_M}{2} & 0 & 0 & 0 \\ -i\frac{\lambda_M}{2} & 0 & 0 & 0 & 0 \\ 0 & 0 & 0 & 0 & 0 \\ 0 & 0 & 0 & 0 & i\frac{\lambda_X}{2} \\ 0 & 0 & 0 & -i\frac{\lambda_X}{2} & 0 \end{pmatrix}. \tag{B8}$$

## APPENDIX C: BAND STRUCTURE OF $MoSe_2$ AND $WSe_2$ FOR THE 11-BAND TBM AND DFT-HSE METHOD

In addition to the two kinds of TMDC materials discussed in the main text, we have included the results for two additional materials in this Appendix. As illustrated in Fig. 11, by employing the parameters from Table V and utilizing our modified TBM, we can still accurately depict the band structure characteristics of $MoSe_2$ and $WSe_2$ as they change with strain.


[1] K. F. Mak and J. Shan, Nat. Photonics **10**, 216 (2016).
[2] Z. Peng, X. Chen, Y. Fan, D. J. Srolovitz, and D. Lei, Light Sci. Appl. **9**, 1 (2020).
[3] R. Roldán, A. Castellanos-Gomez, E. Cappelluti, and F. Guinea, J. Phys.: Condens. Matter **27**, 313201 (2015).
[4] E. Scalise, M. Houssa, G. Pourtois, V. Afanas'ev, and A. Stesmans, Nano Res. **5**, 43 (2012).
[5] J. O. Island, A. Kuc, E. H. Diependaal, R. Bratschitsch, H. S. Van Der Zant, T. Heine, and A. Castellanos-Gomez, Nanoscale **8**, 2589 (2016).
[6] Y. Wang, C. Cong, W. Yang, J. Shang, N. Peimyoo, Y. Chen, J. Kang, J. Wang, W. Huang, and T. Yu, Nano Res. **8**, 2562 (2015).
[7] C. Zhu, G. Wang, B. Liu, X. Marie, X. Qiao, X. Zhang, X. Wu, H. Fan, P. Tan, T. Amand *et al.*, Phys. Rev. B **88**, 121301(R) (2013).
[8] J. Á. Silva-Guillén, P. San-Jose, and R. Roldán, Appl. Sci. **6**, 284 (2016).
[9] J. C. Slater and G. F. Koster, Phys. Rev. **94**, 1498 (1954).
[10] E. Cappelluti, R. Roldán, J. Silva-Guillén, P. Ordejón, and F. Guinea, Phys. Rev. B **88**, 075409 (2013).
[11] R. Roldan, M. P. López-Sancho, F. Guinea, E. Cappelluti, J. A. Silva-Guillén, and P. Ordejon, 2D Mater. **1**, 034003 (2014).
[12] A. C. Dias, F. Qu, D. L. Azevedo, and J. Fu, Phys. Rev. B **98**, 075202 (2018).
[13] A. J. Pearce, E. Mariani, and G. Burkard, Phys. Rev. B **94**, 155416 (2016).
[14] S. Fang, S. Carr, M. A. Cazalilla, and E. Kaxiras, Phys. Rev. B **98**, 075106 (2018).
[15] S. You, H. Kim, and N. Kim, Phys. E **144**, 115400 (2022).
[16] M. Shahriari, A. G. Dezfuli, and M. Sabaeian, Superlattices Microstruct. **125**, 34 (2019).
[17] S. Yuan, R. Roldán, M. Katsnelson, and F. Guinea, Phys. Rev. B **90**, 041402(R) (2014).
[18] A. Castellanos-Gomez, R. Roldán, E. Cappelluti, M. Buscema, F. Guinea, H. S. van der Zant, and G. A. Steele, Nano Lett. **13**, 5361 (2013).
[19] L. Chirolli, E. Prada, F. Guinea, R. Roldán, and P. San-Jose, 2D Mater. **6**, 025010 (2019).
[20] L. Li, E. V. Castro, and P. D. Sacramento, Phys. Rev. B **94**, 195419 (2016).
[21] H. Shi, H. Pan, Y.-W. Zhang, and B. I. Yakobson, Phys. Rev. B **87**, 155304 (2013).
[22] A. Splendiani, L. Sun, Y. Zhang, T. Li, J. Kim, C.-Y. Chim, G. Galli, and F. Wang, Nano Lett. **10**, 1271 (2010).
[23] R. Roldán, J. A. Silva-Guillén, M. P. López-Sancho, F. Guinea, E. Cappelluti, and P. Ordejón, Ann. Phys. **526**, 347 (2014).
[24] B.-Y. Xie, H.-F. Wang, H.-X. Wang, X.-Y. Zhu, J.-H. Jiang, M.-H. Lu, and Y.-F. Chen, Phys. Rev. B **98**, 205147 (2018).
[25] S. Fang, R. K. Defo, S. N. Shirodkar, S. Lieu, G. A. Tritsaris, and E. Kaxiras, Phys. Rev. B **92**, 205108 (2015).
[26] S. Ishihara, T. Egami, and M. Tachiki, Phys. Rev. B **49**, 8944 (1994).
[27] G. Kresse and J. Hafner, Phys. Rev. B **47**, 558 (1993).
[28] G. Kresse and J. Furthmüller, Phys. Rev. B **54**, 11169 (1996).
[29] J. P. Perdew, K. Burke, and M. Ernzerhof, Phys. Rev. Lett. **77**, 3865 (1996).
[30] R. Bromley, R. Murray, and A. Yoffe, J. Phys. C **5**, 759 (1972).
[31] A. Kumar and P. Ahluwalia, Eur. Phys. J. B **85**, 1 (2012).
[32] H. Rostami, R. Roldán, E. Cappelluti, R. Asgari, and F. Guinea, Phys. Rev. B **92**, 195402 (2015).
[33] E. Cappelluti and G. Profeta, Phys. Rev. B **85**, 205436 (2012).

[34] W. A. Harrison, *Elementary Electronic Structure*, revised edition (World Scientific, Singapore, 2004).
[35] C. Tserbak, H. M. Polatoglou, and G. Theodorou, Phys. Rev. B **47**, 7104 (1993).
[36] T. B. Boykin, N. Kharche, and G. Klimeck, Phys. Rev. B **76**, 035310 (2007).
[37] Y.-M. Niquet, D. Rideau, C. Tavernier, H. Jaouen, and X. Blase, Phys. Rev. B **79**, 245201 (2009).
[38] T. B. Boykin, G. Klimeck, R. C. Bowen, and F. Oyafuso, Phys. Rev. B **66**, 125207 (2002).
[39] D. Papaconstantopoulos, M. Mehl, S. Erwin, and M. Pederson, MRS Proc. **491**, 221 (1997).
[40] W. A. Harrison, *Electronic Structure and the Properties of Solids: The Physics of the Chemical Bond* (Dover, New York, 1989).
[41] K. F. Mak, C. Lee, J. Hone, J. Shan, and T. F. Heinz, Phys. Rev. Lett. **105**, 136805 (2010).
[42] A. Raja, A. Chaves, J. Yu, G. Arefe, H. M. Hill, A. F. Rigosi, T. C. Berkelbach, P. Nagler, C. Schüller, T. Korn *et al.*, Nat. Commun. **8**, 15251 (2017).
[43] A. Bhardwaj, J. Kaur, M. Wuest, and F. Wuest, Nat. Commun. **8**, 1 (2017).
[44] J. Heyd, G. E. Scuseria, and M. Ernzerhof, J. Chem. Phys. **118**, 8207 (2003).
[45] T. Cheiwchanchamnangij, W. R. L. Lambrecht, Y. Song, and H. Dery, Phys. Rev. B **88**, 155404 (2013).
[46] H. J. Conley, B. Wang, J. I. Ziegler, R. F. Haglund, Jr., S. T. Pantelides, and K. I. Bolotin, Nano Lett. **13**, 3626 (2013).
[47] B. Aslan, M. Deng, and T. F. Heinz, Phys. Rev. B **98**, 115308 (2018).
[48] S. Yang, W. Chen, B. Sa, Z. Guo, J. Zheng, J. Pei, and H. Zhan, Nano Lett. **23**, 3070 (2023).
[49] M. A. Khan, M. Erementchouk, J. Hendrickson, and M. N. Leuenberger, Phys. Rev. B **95**, 245435 (2017).